CHEMISTRY
A European Journal

A Journal of
ChemPubSoc Europe

Accepted Article

Title: Bio-inspired Architectures and Hetero-Atom Doping to Construct Metal Oxide based Anode for High Performance Lithium Ion Batteries

Authors: Jun Ming, Liming Wang, Qujiang Sun, Lin Zhou, Lianshan Sun, Chunli Wang, Yingqiang Wu, and Xuxu Wang

To be cited as: *Chem. Eur. J.* 10.1002/chem.201804235

Link to VoR: http://dx.doi.org/10.1002/chem.201804235

Supported by
ACES

WILEY-VCH

10.1002/chem.201804235

WILEY-VCH

FULL PAPER

Bio-inspired Architectures and Hetero-Atom Doping to Construct Metal Oxide based Anode for High Performance Lithium Ion Batteries

Qujiang Sun,[a, b] Lin Zhou,[a, c] Lianshan Sun,*[, a] Chunli Wang,[a, c] Yingqiang Wu,*[, d] Xuxu Wang,[a, c] Limin Wang,[a] Jun Ming*[, a]

Abstract: Pursuing the greater energy density and longer life span of lithium ion batteries (LIBs) are urgently needed to satisfy the dramatically increased demand in energy market, where the metal oxide-based anodes are being intensively studied due to the higher capacity over that of current graphite anode. Herein, we introduce a new and sustainable strategy to construct the metal oxide-based anode with high capacity and extremely long cycle life, in which the features of bio-inspired architectures and hetero-atom doping can contribute a lot for great performances. In detail, one-dimensional tube-like metal oxide (*e.g.,* MnO) coated on N-doped carbon framework (*i.e.,* MnO/N-C) is designed using the natural abundant and renewable Metaplexis japonica fibers (MJFs) as the bio-template and hetero-atom sources. Benefiting from the uniqueness of structure and compositions, as-prepared MnO/N-C demonstrates extremely high rate capacities of 951, 777, 497, 435 mAh g^{-1} at the rates of 0.5, 2, 4 and 5 A g^{-1} respectively with a good stability more than 1000 cycles. We find that the electrochemical performances are superior to most previous MnO-based anode, in which the faster kinetics of conversion reactions on the merit of the ion/electron transportation and morphological evolution is verified. We hope that the concept of bio-inspired architectures with hetero-atom doping can be applied in the wider applications for greater capabilities.

Introduction

Rechargeable lithium-ion batteries (LIBs) have dominated the energy market as a power source ranging from portable electronic devices, grid energy storage system to (hybrid) electric vehicles.[1-3] However, the energy density has become a bottle-neck because the limited capacity of lithium metal oxide cathode and graphite anode, such as the low capacity of 372 mAh g^{-1} for graphite anode,[4-6] which are incapable to fulfill the ever-growing demands in energy for further applications.[7-8] Thus, it is challenging and also urgently needed to develop high capacity materials to replace the graphite anode,[9-11] however the guarantee of stability and cycle life are prerequisites before the final commercialization.

Up to now, the metal oxide based anode, such as SiO_x,[12] SnO_x,[13] Fe_2O_3,[14] MnO,[15-16] NiO[17] and Co_3O_4[18] *etc.* are being widely explored because of their higher capacities (>700 mAh g^{-1}) comparing to that of graphite. However, the fatal disadvantages of low electronic conductivity and drastic volumetric expansion during the repeated lithiation/delithiation process seriously hinder their applications.[19-21] To address these issues, reducing the particle size and/or modifying the metal oxide with different kind of carbon are popular strategies to buffer the electrode pulverization and then enhance their capacity and stability.[22-24] Although numerous synthetic strategies including the traditional calcination,[25] carbonization (*e.g.,* if carbon sources were used),[26-27] hydrothermal method[28-30] and sol-gel approach[31-32] have been developed, most approaches always involve too many chemicals; alternatively, there is a popular trend to synthesize metal oxide-based anode from biomaterials (*e.g.,* microalgae,[33] kapok fibers,[34] spirogyra,[35] lotus pollen[36] and *etc.*[37]) to minimize the chemical consumption for sustainability. Distinct from the previous literatures, herein we the first time introduce the Metaplexis japonica fibers (MJFs) as the bio-template to synthesize metal oxide-based anode. The natural abundant Metaplexis japonica can not only offer the unique one-dimensional structure but also can be carbonized to N-doped carbon framework for more intriguing properties. As a result, a new hybrid materials of metal oxide/N-C with hollow structure can be prepared readily in a mass production for diverse applications.

In this study, the metal oxide of MnO is selected as a model not only because of its great advantages, such as the high theoretical capacity of 756 mAh g^{-1} and low electrochemical lithiation force (1.302 V *vs.* Li^+/Li), but also for the abundance and low-cost features.[38-39] Although many excellent researches have been developed for the MnO-based anode,[33-36, 40-42] the electrochemical performance of as-prepared MnO/N-C are superior to most previous materials. In addition, we specifically study the benefits of bio-inspired architectures and hetero-atom doping, in which the faster kinetics of conversion reactions on the merit of ion/electron transportation and morphological evolution is verified. We hope that the presented sustainable strategy can open an avenue to synthesize one-dimensional materials and beyond with the great characteristics like those of carbon nanotubes (CNTs),[43-44] and also the concept of bio-inspired architectures with hetero-atom doping is applicable in other fields (*e.g.,* catalysis, electrochemistry, sensor, electrophonic) for greater performances.

[a] *Q. Sun, L. Zhou, L. Sun, C. Wang, X. Wang, Pro. L. Wang, Pro. J. Ming*
State Key Laboratory of Rare Earth Resource Utilization, Changchun Institute of Applied Chemistry, CAS, Changchun 130022, China
E-mail: lssun@ciac.ac.cn, jun.ming@ciac.ac.cn
[b] *Q. Sun*
University of Chinese Academy of Sciences
Beijing 100049, China
[c] *L. Zhou, L. Sun, C. Wang, X. Wang*
University of Science and Technology of China
Hefei 230026, China
[d] *Y. Wu*
S King Abdullah University of Science and Technology (KAUST)
Physical Sciences and Engineering Division (PSE)
Thuwal 23955-6900, Kingdom of Saudi Arabia
E-mail: yingqiang.wu@kaust.edu.sa

10.1002/chem.201804235
WILEY-VCH

FULL PAPER

Results and Discussion

Features of synthetic strategy and MnO/N-C. The uniqueness of MJFs is shown in **Figure 1**a, in which the white and light fiber change to gray after the biosorption and spontaneous redox deposition of permanganate ion (*i.e.,* $MnO_4^-+3e^-+2H_2O \rightarrow MnO_2+4OH^-$) in $KMnO_4$ aqueous solution.[33] Finally, a black powder was obtained after a thermal treatment, in which crystalline MnO is expected to be coated on N-doped carbon tubes because the MJFs can offer N-doped carbon skeleton after carbonization. The morphology evolution was confirmed in **Figure 2**. The good preservation of tubular structure was demonstrated after the carbonation of raw MJFs, in which the hollow and tubular N-C with the thickness of 400 nm was obtained (**Figure 2**a-b). Benefiting from the robust skeleton, the MnO_2 layer can be de-oxidized in carbonization process (*e.g.,* $2MnO_2+C \rightarrow 2MnO+CO_2$) and then give rise to MnO/N-C micro-tubes with the wall thickness of 500 nm. The MnO nanoparticles with the size of 100-300 nm were coated on the N-C microtubes surface uniformly (**Figure 2**c-f), in which the uniform distribution of Mn, O, C and N in EDS mapping further confirms the efficiency of this strategy to prepare metal oxide/N-C micro-tubes (**Figure 2**g-j). The MnO/N-C has a relatively dense structure, in which the MnO nanograins and carbon matrix contact intimately, giving rise to rich porosity (**Figure 2**k). In addition, the lattice fringes with the interplanar spacing of 0.257 and 0.16 nm correspond well to the (111) and (220) lattice plane of cubic MnO,[38] which also confirms the existence of MnO.

The formation of crystalline MnO is directly confirmed by XRD (**Figure 3**a), in which the diffraction peaks correspond well to the crystal planes of face-centered cubic (*fcc*) MnO (JCPDS No. 07-0230).[42, 45] While the amorphous carbon derived from MJFs can be judged from the weak peak around at 25°.[46] The kind and chemical valence of element were further confirmed by XPS, in which the Mn, O, C, and particularly the N were detected (**Figure 3**b). In detail, the Mn (II) oxidation state was confirmed by the salient banding energy of Mn $2p_{1/2}$ and Mn $2p_{3/2}$ at 653.46 and 641.63 eV with the typical energy difference of 11.8 eV[47] (**Figure 3**c). The information of C and N were summarized in high resolution spectrum. The first, the prominent peak at 284.55 eV in

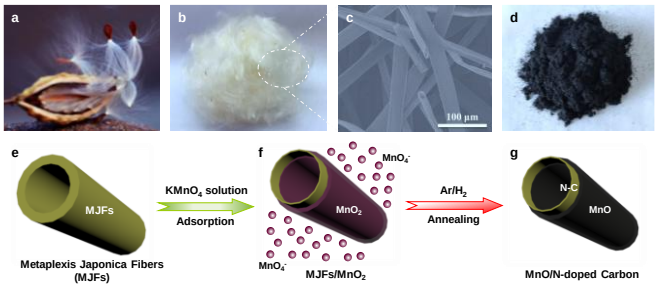

Figure 1. Schematic of the synthetic process. (a, b) Digital photograph and SEM image of raw Metaplexis japonica fibers (MJFs). (d) Photograph of as-prepared MnO/N-C. (e-f) Illustration of procedures from MJFs to for MnO/N-C.

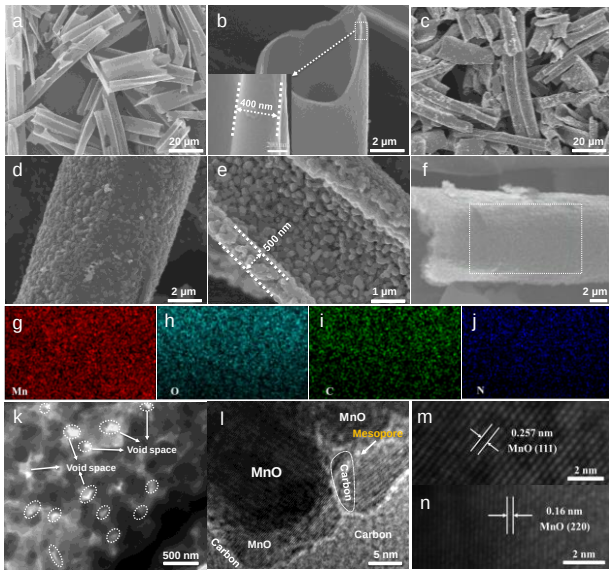

Figure 2. FESEM images of (a-b) carbonized MJFs (e.g., N-C) and (c-e) MnO/N-C at different magnification; (f) Represented SEM image and (g-j) element mapping images of MnO/N-C; (k) TEM and (l-n) HRTEM images of MnO/N-C.

C 1s spectrum assigns to sp^2-hybridized graphitic carbon (C=C), whereas the signals at 285.46 and 288.52 eV correspond to the C-N and C=O configurations respectively.[16,48] Besides, there are two kinds of N in MnO/N-C, namely, pyrrolic N (399.9 eV), pyridinic N (398.35 eV),[47] as shown in N 1s spectrum (**Figure 3**d). Note that the full coating of MnO on N-C framework can be further identified in Raman spectroscopy (**Figure 3**e), where the D-band and G-band of carbon almost disappear even the N-C content in MnO/N-C is still as high as 13.9% (**Figure S2**); meanwhile the two vibrational bands at 566.9 and 641.5 cm^{-1} also confirms the existence of MnO.[33] The porous characteristics of MnO/N-C was determined by N_2 adsorption/desorption measurements (**Figure 3**f). The type-I isotherm with a hysteresis loop demonstrates the existence of micro- and meso-pores, based on which a high specific surface area of 169.5 $m^2\ g^{-1}$ with the pore size distribution of 0.94 nm were confirmed.

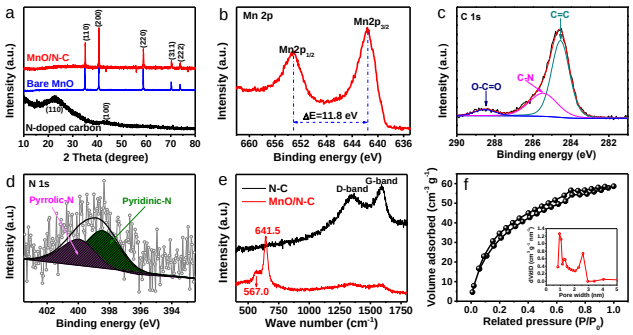

Figure 3. (a) XRD patterns of MnO/N-C, bare MnO and N-C. High-resolution XPS spectra of (b) Mn 2p, (c) C 1s and (d) N 1s in MnO/N-C. (e) Raman spectra and (f) N_2 adsorption/desorption isotherm of MnO/N-C.

10.1002/chem.201804235

Electrochemical Performances. The lithium storage capabilities of MnO/N-C are evaluated first. The superiorities of MnO/N-C over that of bare MnO and N-C is demonstrated in **Figure 4**a. The MnO/N-C delivers an extremely high capacity of 890 mAh g^{-1} at 0.5 A g^{-1} in initial 200 cycles, which is much higher than 396 mAh g^{-1} of bare MnO and 233 mAh g^{-1} of N-C. The capacity of MnO/N-C is much higher than the theoretical value of 756 mAh g^{-1} for MnO, which should be benefit from the lithium storage capability within the spaces of nanostructures. The fine (dis-)charge curves of MnO/N-C were presented in **Figure 4**b, where the increased capacity may result from the activation of MnO during the cycling for the repeated (de-)lithiation.[39, 49] One interesting phenomenon we find that the bare MnO has no increment trend in capacity comparing to that of MnO/N-C. This confirms the importance of N-C, because the N-C can offer higher electronic conductivity and also disperse the (dis-)charge products efficiently for the activation of metal oxide. The increased trend of capacity and its stability were further confirmed by the cyclic voltammetry in **Figure 4**c. We find that the MnO/N-C based electrode can be activated after the 1st scan and then the position of redox peaks was stabilized fast afterwards. Note that the better rate capacities of MnO/N-C over those of bare MnO and N-C is further confirmed in **Figure 4**d. For example, the rate capacities of 951, 905, 703, 497, and 348 mAh g^{-1} are obtained for the MnO/N-C at the current densities of 0.1, 0.5, 2.0, 4.0, and 5.0 A g^{-1} respectively, which is much higher than 704, 607, 510, 372, 237 mAh g^{-1} of MnO and 391, 215, 156, 130, 110 mAh g^{-1} of N-C. The comparative results fully confirm the merits of MnO/N-C benefiting from the bio-inspired architectures and hetero-atom compositions of N-C.

Herein, the fast reaction rate (*i.e.,* kinetics) of lithium with MnO/N-C is further confirmed by the rate test in discharge, in which high capacities of 797, 768, 699, and 682 mAh g^{-1} can be delivered at the current densities of 1, 2, 4, and 5 A g^{-1}, respectively (**Figure 4**e) when the charge current density was fixed at 0.1 A g^{-1}. Conversely, the release of lithium from the lithiated MnO/N-C is studied as varying the charged current density from 0.2 to 5 A g^{-1} under the constant discharged current density of 0.2 A g^{-1} (**Figure 4**f). We find that the charged capacities are 887, 848, 811, 758, 716, and 711 mAh g^{-1} respectively, which has minor differences comparing to the discharged capacities of 925, 911, 862, 799, 768, and 728 mAh g^{-1}. These results all demonstrate the fast discharge and charge rate during the reactions, which are consistence with the good rate capabilities. Note that, another great feature of MnO/N-C is the long-term cycling stability. For example, the MnO/N-C can cycle more than 300, 500 and 1000 cycles respectively under the current densities of 1, 2 and 5 A g^{-1}, where the average capacity is as high as 1002, 777 and 435 mAh g^{-1} respectively (**Figure S3-S4**). In addition, the specific capacity exhibits the "decrease-increase" trend (**Figure 4**g), which can be attribute to the activation of MnO and be related to the generation of higher oxidation state manganese (*e.g.,* Mn^{3+}/Mn^{4+}) during the charge/discharge process. As a result, the MnO/N-C demonstrates the superior performances comparing to most MnO-based anode reported previously (**Figure 5**).[27, 33, 35-37, 40-41, 50-58]

Electrochemical analysis. Except the benefit of architectures and hetero-atom doping, the improved electronic conductivity of MnO/N-C is another reason for the greater performance, as confirmed in EIS (**Figure 6**a-b). The charge transfer resistance (R_{ct}) of MnO/N-C (i.e., 81.3 Ω) is much lower than 137.2 Ω of bare MnO, which can convenient the faster reactions over that of bare MnO. And also, we find that the R_{ct} value of MnO/N-C electrode decreases gradually as cycling (*e.g.,* 30.3 and 24.3 Ω at 100th and 500th cycle respectively, **Figure 6**b). It demonstrates the better contact of MnO/N-C within electrode and the conveniences of further activation for the higher capacity. Besides, the diffusion coefficient of lithium ions (D_{Li+}) was calculated and compared through the following equation: [59]

$$D_{Li} = \frac{R^2T^2}{2A^2n^4F^4C^2\sigma^2}$$

where R is the gas constant, T is the absolute temperature, A is the surface area of the anode, n is the number of electrons per molecule during oxidation, F is the Faraday constant, C is the concentration of lithium ion, and σ is the Warburg coefficient, which can obtained by the linear fitting of Z' versus $\omega^{-1/2}$ (*i.e.,* $Z' = (R_0 + R_{ct}) + \sigma\omega^{-1/2}$),[60] as shown in **Figure S5**. We find that the diffusion coefficient of lithium ions (D_{Li+}) for MnO/N-C (*i.e.,* 3.54 × 10^{-13} cm^2 s^{-1}) is much higher than 1.22 × 10^{-14} cm^2 s^{-1} of bare MnO (**Figure S6**). The improved D_{Li+} should be ascribed to the rich pores in N-doped carbon and reduced MnO particle size, which can facilitate the penetration of electrolyte for Li^+ migration and also shorten the Li^+ diffusion path within particles.

The capacity contribution and electrochemical transport kinetics of MnO/N-C were further analyzed by the CV to understand the high performances (**Figure 6**c). Herein, three peaks named as peak 1, peak 2 and peak 3 (wherein peak 3

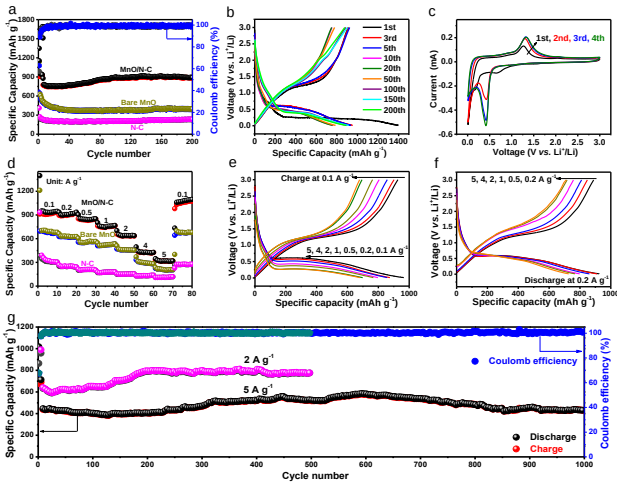

Figure 4. (a) Comparative cycle performances of MnO/C-N, bare MnO and N-C at the current density of 0.5 A g^{-1}. (b) Voltage *vs.* capacity profiles at the current density of 0.5 A g^{-1} and (c) cyclic voltammetry of MnO/C-N. (d) Comparative rate capabilities of MnO/N-C, MnO, and N-C electrodes. (e) Voltage *vs.* capacity profile of MnO/N-C at the current density of 0.1-5 A g^{-1} under the constant current density of 0.1 A g^{-1} in charge. (f) Voltage *vs.* capacity profile of MnO/N-C at 0.2 A g^{-1} in discharge under the charged current density of 0.2-5 A g^{-1}. (g) Cycling performance of MnO/N-C at the current densities of 2 and 5 A g^{-1}.

10.1002/chem.201804235

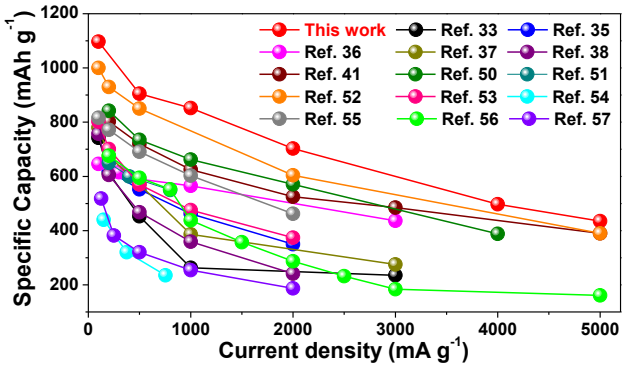

Figure 5. Comparison of the rate performance of previously reported MnO/C anode materials with our work.

means the oxidation of Mn^{2+} to a higher oxidation state of Mn^{4+} during Li^+ ion extraction process)[27] are selected to identify the relationship between the peak current (*i*) and scan rate (*v*) in a sweep voltammetry measurement: $i = av^b$, wherein a and b are both constants.[61-64] We find that the b-value for the MnO/N-C electrode at the peaks 1, 2, and 3 are 0.73, 0.70 and 0.87 respectively, as calculated from the slope of the *log i* versus *log v* plot in **Figure 6**d. According to the classification of b-value (*i.e.,* 0.5<b<1), the MnO/N-C electrode has a combined behavior of diffusion-controlled Li^+ insertion process (*i.e.,* b=0.5) and surface-controlled charge storage behavior (*i.e.,* b=1).[65] As a result, the contribution of battery behavior and capacitance can be quantitatively calculated by dividing the total current *i* into diffusion-controlled part (proportional to $v^{1/2}$) and capacitive part (proportional to the scan rate *v*):

$$i = k_1 v + k_2 v^{1/2}$$ (k_1 and k_2 are constants).[63]

Wherein the k_1 and k_2 can be obtained by plotting $iv^{-1/2}$ versus $v^{1/2}$. Based on the analysis, several results we can summarize: *i*) the capacity contribution resulting from the diffusion-controlled battery behaviors maintains around 29.6-15.9% as increasing the sweep rate from 0.3-1.5 mV s^{-1}. The difference is not that kind of

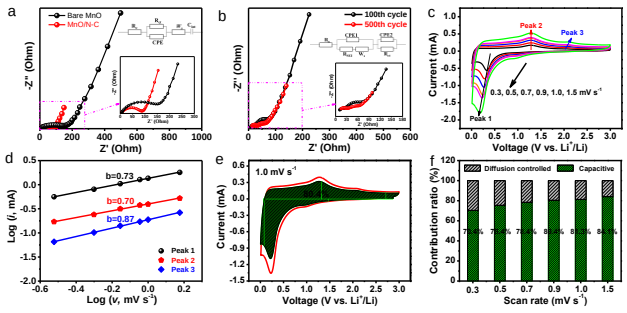

Figure 6. Nyquist plots of (a) MnO/N-C and bare MnO electrode and (b) cycled MnO/N-C electrodes at the current density of 2 A g^{-1}. Insets are the model of the equivalent circuit, and the impedance spectrum of the electrodes at high frequency region. Quantitative capacitive analysis of lithium storage behavior. (c) CV of MnO/N-C electrode at different scan rates. (d) Relationship between logarithm cathodic peak current and logarithm scan rates. (e) Capacitive contribution (Green) and diffusion contribution at 1.0 mV s^{-1}. (f) Normalized contribution ratio of capacitive capacities at different scan rates.

obvious,[63] and one of the reasons should be ascribed to the faster lithium diffusion constant within the MnO/N-C; ii) the capacitive contribution dominates the capacity contribution and the value is as high as 70.4% at the sweep rate of 0.3 mV s^{-1}, which can further increase to 84.1% at 1.5 mV s^{-1} (**Figure 6**f). The results demonstrate that the unique bio-inspired architectures (*e.g.,* high surface area) and hetero-atom doping (*e.g.,* more active site)[66] is the root cause for the high capacity and robust rate capabilities.

Electrode evolution and analysis. The MnO/N-C electrode after cycle are examined to analyze the structural evolution. The first, we find that the electrode can be well preserved without any obvious collapse and pulverization after the cycling (**Figure 7**a). It demonstrates that the MnO/N-C micro-tubes can buffer the volumetric variation efficiently. And also, the original morphology is almost maintained and the MnO nanograins are still anchored on the N-C framework closely during the cycling (**Figure 7**b), demonstrating their good contact and positive effect to maintain the high electronic conductivity. Note that the size of MnO nanograins reduced comparing to those of pristine one and it may result from the pulverization in repeated (de-)lithiation process. This phenomenon is consistence with the observed increment trend of capacity as cycling, in which the reduced MnO particles is easy for further activation and then give rise to increased capacity. After running more than 500 cycles, the lattice fringes of samples have the interplanar spacing of 0.258 nm and 0.219 nm and they still correspond well to the (111) and (200) lattice planes of MnO (**Figure 7**c), confirming the reversible reaction of MnO in

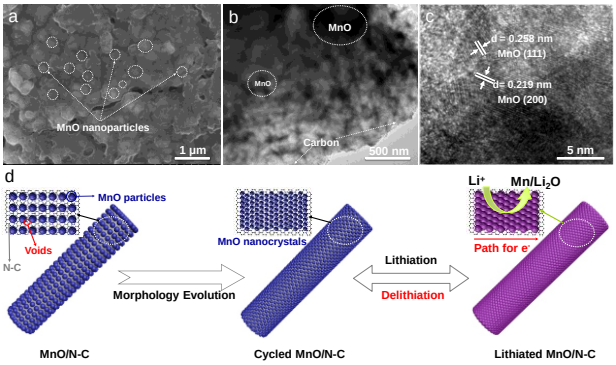

Figure 7. (a) FESEM, (b) TEM and (c) HRTEM images of MnO/N-C electrode after 500th cycle at 2 A g^{-1}. (d) Schematic illustration of morphological evolution and lithium storage process of MnO/N-C electrode.

the repeated (dis-)charge process. The comparative results show that the high performances result from the one-dimensional N-C framework, which can not only offer the fast-electronic transportation capability for the supported MnO nanograins, but also the hollow tubes/porosity can facilitate the Li^+ ions diffusion, thus giving rise to the faster kinetics of conversion process, as summarized in **Figure 7**d.

Conclusions

In summary, a sustainable strategy is presented to design a new metal oxide-based hybrid using renewable MJFs as the bio-

template, based on which one-dimensional MnO/N-C micro-tubes is prepared and it demonstrates extremely high lithium storage capabilities and long cycle life as an anode. For example, impressive capacities of 905, 777, 497 and 435 mAh g^{-1} can be delivered at the current density of 0.5, 2, 4 and 5 A g^{-1} respectively with a good stability more than 1000 cycles. The electrochemical performances of MnO/N-C are superior to most previous results, in which the faster kinetics of conversion process on the metis of the ion/electronic transportation and morphological evolution from the one-dimensional N-C frameworks is verified in detail. Our results show that developing the bio-inspired architectures with hetero-atom doping are efficient approach to construct the functional materials with greater performances, and we hope this kind of concept can be applied in the wider fields for diverse applications.

Experimental Section

Synthetic Procedures. The Metaplexis japonica fibers (MJFs) was collected in nature and washed with acetone, ethanol and deionized water (DIW) several times to remove the impurities before the vacuum freeze-dry. Then, 0.5 g MJFs was added to 200 mL 0.3 M $KMnO_4$ (A.R., >99.5%) aqueous solution and stirred for 8 h at room temperature. The intermediates of MJFs/Mn-based species were collected after the filtration and freeze-dry. Finally, the hybrid MnO/N-C micro-tubes was obtained through the calcination at 700 ºC for 5 h under a flow of Ar, where the heating rate is controlled at 3 ºC min^{-1}.

Materials characterization. The crystalline information was acquired by X-ray diffractometer (XRD, Bruker D8 Focus) at a scan speed of 2° min^{-1} with copper Kα radiation. The morphology was characterized by scanning electron microscope images (SEM) operating on field emission Hitachi S-4800 instrument at the accelerating voltage of 10 kV. The structural information and element mapping were observed by transmission electron microscopy (TEM) and high-angle annular dark-field scanning transmission electron microscopy (HAADF-STEM) on FEI Tecnai G2 S-Twin instrument with field emission gun operating at 200 kV. The carbon content in composite was analyzed by thermogravimetric (TG) analysis within the temperature of 25-800 ºC with the heating rate of 10 ºC min^{-1} under air flow using the STA 449 Jupiter (NETZSCH) thermogravimetry analyser. The BET surface area and porosity were determined by N_2 adsorption/desorption measurements conducted with Micromeritics ASAP 2010 instrument at -196 ℃ after the sample was degassed at 200 ºC for 6 h under vacuum conditions. The pore size distribution curves were estimated from the adsorption isotherms using the Barrett–Joyner–Halenda (BJH) method.

Electrochemical measurements. The working electrode was prepared as below. The active material of MnO/N-C, carbon black and poly(vinylidene fluoride) (PVDF) with the mass ratio of 7:2:1 were mixed in N-methyl-2-pyrrolidone to form a uniform slurry and then casted on copper foil. The electrode was vacuum-dried at 80 ºC overnight, and the areal mass density of active material was controlled at 1.12 mg cm^{-2}. The CR 2025 coin-type cell has the configuration of working electrode | Celgard 2400 membrane separator | metallic lithium foil, in which the electrolyte of 1.0M $LiPF_6$ in ethyl carbonate/diethyl carbonate (1:1, *v/v*) was used. The cell was assembled in glovebox, in which the moisture and oxygen were strictly controlled below 0.1 ppm. Galvanostatic charge-discharge performances were measured under the cut-off voltage of 0.01-3 V (*vs*. Li/Li^+) using the Land battery testing system at room temperature. Cyclic voltammetry (CV) measurement was conducted on BioLogic VMP3 electrochemical workstation at the scan rate of 0.1 mV s^{-1}, and the electrochemical impedance spectroscopy (EIS) was carried out within the range of 10 mHz-100 kHz with an applied amplitude of 5 mV.

Acknowledgements

This work is supported by the National Natural Science Foundation of China (21521092).

Keywords: Bio-inspired materials • metal oxide • anode • hetero-atom doping • Li-ion batteries

References

[1] M. Arm, J. M. Tarascon, *Nature* **2008**, 451, 652-657.
[2] B. Dunn, H. Kamath, J. M. Tarascon, *Science* **2011**, 334, 928-935.
[3] J. B. Goodenough, *Nat. Electron.* **2018**, 1, 204-204.
[4] Y. P. Wu, E. Rahm, R. Holze, *J. Power Sources* **2003**, 114, 228-236.
[5] A. D. Roberts, X. Li, H. Zhang, *Chem. Soc. Rev.* **2014**, 43, 4341-4356.
[6] J. Ming, Z. Cao, W. Wahyudi, M. Li, P. Kumar, Y. Wu, J.-Y. Hwang, M.N. Hedhili, L. Cavallo, Y.-K. Sun, L. J. Li, *ACS Energy Lett.* **2018**, 3, 335-340.
[7] B. Scrosati, J. Hassoun, Y. K. Sun, *Energy Environ. Sci.* **2011**, 4, 3287-3295.
[8] J. Ming, M. Li, P. Kumar, A.-Y. Lu, W. Wahyudi, L. J. Li, *ACS Energy Lett.* **2016**, 1, 529-534.
[9] J. Cabana, L. Monconduit, D. Larcher, M. R. Palacin, *Adv. Mater.* **2010**, 22, E170-192.
[10] H. Ming, J. Ming, S. M. Oh, S. Tian, Q. Zhou, H. Huang, Y. K. Sun, J. Zheng, *ACS Appl. Mater. Interfaces* **2014**, 6, 15499-15509.
[11] H. Ming, J. Qiu, S. Zhang, M. Li, X. Zhu, L. Wang, J. Ming, *ChemElectroChem.* **2017**, 4, 1165-1171.
[12] Y. S. Hu, R. Demir-Cakan, M. M. Titirici, J. O. Muller, R. Schlogl, M. Antonietti, J. Maier, *Angew Chem. Int. Ed.* **2008**, 47, 1645-1649.
[13] G. D. Park, J.-K. Lee, Y. C. Kang, *Adv. Funct. Mater.* **2017**, 27, 1603399-1603408.
[14] D. Kong, C. Cheng, Y. Wang, B. Liu, Z. Huang, H. Y. Yang, *J. Mater. Chem. A* **2016**, 4, 11800-11811.
[15] W. Zhang, J. Sheng, J. Zhang, T. He, L. Hu, R. Wang, L. Mai, S. Mu, *J. Mater. Chem. A* **2016**, 4, 16936-16945.
[16] Y. Zhang, P. Chen, X. Gao, B. Wang, H. Liu, H. Wu, H. Liu, S. Dou, *Adv. Funct. Mater.* **2016**, 26, 7754-7765.
[17] G. Huang, D. Yin, F. Zhang, Q. Li, L. Wang, *Inorg. Chem.* **2017**, 56, 9794-9801.
[18] K. Zhang, P. Li, M. Ma, J. H. Park, *Adv. Funct. Mater.* **2016**, 26, 2959-2965.
[19] J. Ming, Y. Wu, G. Liang, J.-B. Park, F. Zhao, Y. K. Sun, *Green Chem.* **2013**, 15, 2722-2726.
[20] J. Zhang, W. Zhang, T. He, I. S. Amiinu, Z. Kou, J. Li, S. Mu, *Carbon* **2017**, 115, 95-104.
[21] L. Zhou, Y. Cheng, Q. Sun, L. Sun, C. Wang, X. Wang, D. Yin, L. Wang, J. Ming, *Chem. Commun.* **2018**, 54, 4049-4052.
[22] M. V. Reddy, G. V. Subba Rao, B. V. Chowdari, *Chem. Rev.* **2013**, 113, 5364-5457.
[23] J. Ming, Y. Wu, J. B. Park, J. K. Lee, F. Zhao, Y. K. Sun, *Nanoscale* **2013**, 5, 10390-10396.
[24] X. Ding, X. Huang, J. Jin, H. Ming, L. Wang, J. Ming, *Electrochim Acta* **2018**, 260, 882-889.
[25] R. Verrelli, J. Hassoun, *ChemElectroChem.* **2015**, 2, 988-994.

[26] H. Ming, J. Ming, S.-M. Oh, E. J. Lee, H. Huang, Q. Zhou, J. Zheng, Y.-K. Sun, *J. Mater. Chem. A* **2014**, 2, 18938-18945.
[27] S. Wang, Y. Xing, C. Xiao, H. Xu, S. Zhang, *J. Power Sources* **2016**, 307, 11-16.
[28] Y. Cheng, Q. Li, C. Wang, L. Sun, Z. Yi, L. Wang, *Small* **2017**, 13, 1701993-1702003..
[29] X. Ding, X. Huang, J. Jin, H. Ming, L. Wang, J. Ming, *J. Power Sources* **2018**, 379, 53-59.
[30] G.Q. Zhang, X.W. Lou, Angew Chem. Int. Ed. **2014**, 47, 9187-9190.
[31] J. Ming, J. B. Park, Y. K. Sun, *ACS Appl. Mater. Interfaces* **2013**, 5, 2133-2136.
[32] G. Sun, H. Xie, J. Ran, L. Ma, X. Shen, J. Hu, H. Tong, *J. Mater. Chem. A* **2016**, 4, 16576-16587.
[33] Y. Xia, Z. Xiao, X. Dou, H. Huang, X. H. Lu, R. J. Yan, Y. P. Gan, W. J. Zhu, J. P. Tu, W. K. Zhang, X. Y. Tao, *ACS Nano* **2013**, 7, 7083–7092.
[34] X. Tao, W. Chai, F. Xu, J. Luo, H. Xiao, C. Liang, Y. Gan, H. Huang, Y. Xia, W. Zhang, *Electrochim Acta* **2015**, 169, 159-167.
[35] J. Wang, W. Liu, J. Chen, H. Wang, S. Liu, S. Chen, *Electrochim Acta* **2016**, 188, 210-217.
[36] W. Zhu, H. Huang, W. Zhang, X. Tao, Y. Gan, Y. Xia, H. Yang, X. Guo, *Electrochim Acta* **2015**, 152, 286-293.
[37] C. Yang, Q. Gao, W. Tian, Y. Tan, T. Zhang, K. Yang, L. Zhu, *J. Mater. Chem. A* **2014**, 2, 19975-19982.
[38] H. Jiang, Y. J. Hu, S. J. Guo, C. Y. Yan, P. S. Lee, C. Z. Li, *ACS Nano* **2014**, 8, 6038-6046.
[39] T. Yuan, Y. Jiang, W. Sun, B. Xiang, Y. Li, M. Yan, B. Xu, S. Dou, *Adv. Funct. Mater.* **2016**, 26, 2198-2206.
[40] L. F. Chen, S.-X. Ma, S. Lu, Y. Feng, J. Zhang, S. Xin, S. H. Yu, *Nano Res.* **2017**, 10, 1-11.
[41] H. Z. Yang, W. Liu, Y. Zhang, H. L. Wang, S. Liu, S. G. Chen, F. L. Cheng, S. P. Zhao, E. C. Hao, *ChemElectroChem.* **2017**, 4, 1411-1418.
[42] H. Wang, Z. Xu, Z. Li, K. Cui, J. Ding, A. Kohandehghan, X. Tan, B. Zahiri, B. C. Olsen, C. M. Holt, D. Mitlin, *Nano Lett.* **2014**, 14, 1987-1994.
[43] W. D. Zhang, B. Xu, L. C. Jiang, *J. Mater. Chem.* **2010**, 20, 6383-6391.
[44] W. Wahyudi, Z. Cao, P. Kumar, M. Li, Y. Wu, M. N. Hedhili, T. D. Anthopoulos, L. Cavallo, L. J. Li, J. Ming, *Adv. Funct. Mater.* **2018**, DOI: 10.1002/adfm.201802244, 1802244-1802252.
[45] C. Chae, J. H. Kim, J. M. Kim, Y.-K. Sun, J. K. Lee, *J. Mater. Chem.* **2012**, 22, 17870-17877.
[46] D. G. Lim, K. Kim, M. Razdan, R. Diaz, S. Osswald, V. G. Pol, *Carbon* **2017**, 121, 134-142.
[47] S. Petnikota, V. V. S. S. Srikanth, P. Nithyadharseni, M. V. Reddy, S. Adams, B. V. R. Chowdari, *ACS Sustain. Chem. Eng.* **2015**, 3, 3205-3213.
[48] B. Y. Xia, Y. Yan, N. Li, H. B. Wu, X. W. Lou, X. Wang, *Nat. Energy* **2016**, 1, 15006.
[49] H. Ming, H. Zhou, X. Zhu, S. Zhang, P. Zhao, M. Li, L. Wang, J. Ming, *Energy Technol.* **2018**, 6, 766-772.
[50] F. Cheng, W. C. Li, A. H. Lu, *ACS Appl. Mater. Interfaces* **2016**, 8, 27843-27849
[51] J. Guo, Q. Liu, C. Wang, M. R. Zachariah, *Adv. Funct. Mater.* **2012**, 22, 803-811.
[52] L. Sheng, S. Liang, T. Wei, J. Chang, Z. Jiang, L. Zhang, Q. Zhou, J. Zhou, L. Jiang, Z. Fan, *Energy Storage Mater.* **2018**, 12, 94-102.
[53] J. G. Wang, H. Liu, H. Liu, Z. Fu, D. Nan, *Chem. Eng. J.* **2017**, 328, 591-598.
[54] Y. Liu, X. Zhao, F. Li, D. Xia, *Electrochim Acta* **2011**, 56, 6448-6452.
[55] X. Li, S. Xiong, J. Li, X. Liang, J. Wang, J. Bai, Y. Qian, *Chem. Eur. J.* **2013**, 19, 11310-11319.
[56] H. Hu, H. Cheng, Z. Liu, Y. Yu, *Electrochim Acta* **2015**, 152, 44-52.
[57] H. Liu, Z. Li, Y. Liang, R. Fu, D. Wu, *Carbon* **2015**, 84, 419-425.
[58] Y.M. Sun, X.L. Hu, W. Luo, F.F. Xia, Y.H. Huang, *Adv. Funct. Mater.* **2013,** 23, 2436-2444.
[59] L. Hu, J. Yang, I. S. Amiinu, X. Kang, W. Zhang, S. Mu, *J. Mater. Chem. A* **2015**, 3, 23368-23375.
[60] Q. Cao, H. P. Zhang, G. J. Wang, Q. Xia, Y. P. Wu, H. Q. Wu, *Electrochem. Commun.* **2007**, 9, 1228-1232.
[61] V. Augustyn, P. Simon, B. Dunn, *Energy Environ. Sci.* **2014**, 7, 1597.
[62] H. S. Kim, J. B. Cook, H. Lin, J. S. Ko, S. H. Tolbert, V. Ozolins, B. Dunn, *Nat. Mater.* **2017**, 16, 454-460.
[63] V. Augustyn, J. Come, M. A. Lowe, J. W. Kim, P. L. Taberna, S. H. Tolbert, H. D. Abruna, P. Simon, B. Dunn, *Nat. Mater.* **2013**, 12, 518-522.
[64] J.Y. Gao, Y.P. Li, L. Shi, J.J. Li, G.Q. Zhang, *ACS Appl. Mater. Interfaces* **2018**, 10, 20635-20642.
[65] B. K. Lesel, J. S. Ko, B. Dunn, S. H. Tolbert, *ACS Nano* **2016**, 10, 7572-7581.
[66] H. Xue, Z. Na, Y. Wu, X. Wang, Q. Li, F. Liang, D. Yin, L. Wang, J. Ming, *J. Mater. Chem. A* **2018**, 6, 12466–12474.

10.1002/chem.201804235

WILEY-VCH

FULL PAPER

A new and sustainable strategy is introduced to construct the metal oxide-based anode with high capacity and extremely long cycle life, in which the features of bio-inspired architectures and hetero-atom doping can contribute a lot for the greater performances.

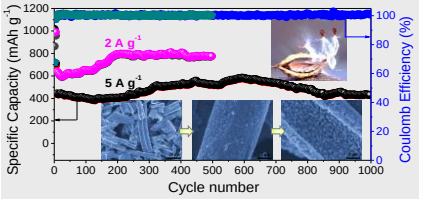

Qujiang Sun,[a, b] Lin Zhou,[a, c] Lianshan Sun,[, a] Chunli Wang,[a, c] Yingqiang Wu,[*, d] Xuxu Wang,[a, c] Limin Wang,[a] Jun Ming[*, a]*

Page 1. – Page 6.

Bio-inspired Architectures and Hetero-Atom Doping to Construct Metal Oxide based Anode for High Performance Lithium Ion Batteries